Pharmaceutical Research, Vol. 27, No. 11, November 2010 (© 2010)
DOI: 10.1007/s11095-010-0068-z

Research Paper

In Vivo Distribution of Polymeric Nanoparticles at the Whole-Body, Tumor, and Cellular Levels

Helen Lee,[1] Bryan Hoang,[1] Humphrey Fonge,[1] Raymond M. Reilly,[1,2,3] and Christine Allen[1,4,5,6]

Received September 29, 2009; accepted January 11, 2010; published online March 2, 2010

Purpose. Block copolymer micelles (BCMs) were functionalized with indium-111 and/or epidermal growth factor (EGF), which enabled investigation of the *in vivo* transport of passively and actively targeted BCMs. The integration of conventional and image-based techniques afforded novel quantitative means to achieve an in-depth insight into the fate of polymeric nanoparticles *in vivo*.
Methods. Pharmacokinetics and biodistribution studies were performed in athymic mice bearing human breast xenografts to evaluate the whole-body transport of NT-BCMs (non-targeted, EGF-) and T-BCMs (targeted, EGF+). The intratumoral distribution of BCMs was investigated using MicroSPECT/CT and autoradiographic imaging, complemented with quantitative MATLAB® analyses. Tumors were fractionated for quantifying intracellular uptake of BCMs via γ-counting.
Results. The intratumoral distribution of NT-BCMs and T-BCMs were found to be heterogeneous, and positively correlated with tumor vascularization ($r>0.68\pm0.04$). The enhanced *in vivo* cell uptake and cell membrane binding of T-BCMs were found to delay their clearance from tumors overexpressing EGFR, and therefore resulted in enhanced tumor accumulation for the T-BCMs in comparison to the NT-BCMs.
Conclusions. Adequate passive targeting is required in order to achieve effective active targeting. Tumor physiology has a significant impact on the transvascular and intratumoral transport of passively and actively targeted BCMs.

KEY WORDS: active targeting; block copolymer micelles; epidermal growth factor; intratumoral distribution; passive targeting.

INTRODUCTION

Nanoparticle-based drug delivery systems (NDDS) have made an enormous impact in the field of drug formulation, especially in oncology, with many drugs relying on NDDS currently in clinical trials or with approval for clinical use (1,2). In particular, long-circulating NDDS have the ability to passively target solid tumors via the enhanced permeability and retention (EPR) effect. The EPR effect occurs as a result of the leaky vasculature and impaired lymphatic clearance within tumors, which leads to preferential NDDS extravasation and retention at the tumor site (3). Compared to free drugs of lower molecular weight, drugs encapsulated in long-circulating NDDS exhibit more favorable pharmacokinetics, biodistribution, and toxicity profiles (4–6). In an attempt to further increase the therapeutic index of drug-loaded NDDS, many scientists have pursued active targeting by functionalizing the NDDS surface with moieties that recognize biomarkers expressed in diseased tissues. Examples of active targeting biomarkers include receptors for ligands with high affinity for angiogenic neovasculature (7,8) or proliferation markers that are overexpressed on the tumor cell surface (9–11). Several excellent reviews on the recent progress of actively targeted NDDS can be found elsewhere (12,13).

The most established molecular targets exploited in the development of actively targeted NDDS for oncology include the folate (14,15), HER-2 (9,16), and epidermal growth factor (EGF) receptors (10,17,18). The popularity of these molecular targets stems from their overexpression in a wide range of tumor cells, as well as their well-characterized biological functions and internalization pathways. Upon binding to their corresponding receptors, internalization of the ligand-conjugated NDDS occurs rapidly and, therefore, significantly enhances intracellu-

[1] Department of Pharmaceutical Sciences, Leslie Dan Faculty of Pharmacy, University of Toronto, 144 College St., Toronto, Ontario, Canada M5S 3M2.
[2] Division of Nuclear Medicine, University Health Network, University of Toronto, 144 College St., Toronto, Ontario, Canada M5S 3M2.
[3] Department of Medical Imaging, Faculty of Medicine, University of Toronto, 144 College St., Toronto, Ontario, Canada M5S 3M2.
[4] Department of Chemistry, Faculty of Arts and Science, University of Toronto, 144 College St., Toronto, Ontario, Canada M5S 3M2.
[5] STTARR Innovation Centre, Radiation Medicine Program, Princess Margaret Hospital, University Health Network, Toronto, Ontario, Canada.
[6] To whom correspondence should be addressed. (e-mail: cj.allen@utoronto.ca)

ABBREVIATIONS: BCM, Block copolymer micelle; EGF, Epidermal growth factor; EGFR, Epidermal growth factor receptors; h.p.i., Hours post-injection; IFP, Interstitial fluid pressure; NDDS, Nanoparticle-based drug delivery system; NT, Non-targeted; PEG-*b*-PCL, Poly (ethylene glycol)-*block*-poly(ε-caprolactone); SPECT/CT, Single photon emission computed tomography/Computed tomography; T, Targeted; TAM, Tumor-associated macrophages; ^{111}In, Indium-111.

lar transport. Numerous studies have examined the *in vitro* uptake of targeted NDDS (T-NDDS) *versus* non-targeted NDDS (NT-NDDS) (12,19,20). Many drug-loaded T-NDDS have shown promise *in vitro*, where significant increases in cellular uptake along with much improved cytotoxicity were observed when compared to their NT counterparts (11,17,21). Most *in vivo* studies have focused on examining the pharmacokinetics, biodistribution profiles, and therapeutic efficacy, of T- and NT-NDDS in tumor-bearing animals. However, few studies have investigated the *in vivo* cellular uptake of T- and NT-NDDS in order to determine if the promising results obtained for cell uptake *in vitro* are reproducible *in vivo*. More importantly, knowledge regarding the intratumoral distribution and tumor penetration of NDDS following passive and/or active targeting is limited. While a few reports on liposome-based formulations (9,15) have begun to shed light on some questions pertaining to the fate of T- and NT-NDDS *in vivo*, the tissue and cellular transport of polymeric nanoparticles, such as block copolymer micelles (BCMs), remain virtually unexplored.

The current study aims to elucidate the tumor accumulation kinetics, intratumoral distribution, and *in vivo* cellular uptake of BCMs. The BCMs were labeled with indium-111 (^{111}In) for *in vivo* tracking, while T-BCM surfaces were also functionalized with EGF as a targeting moiety, which is an endogenous ligand for the EGF receptor (EGFR). EGFR is overexpressed in a wide range of epithelial cancers, including lung and breast (22,23). Our group has previously reported that T-BCMs (EGF-conjugated BCMs) loaded with an anticancer drug exhibit enhanced *in vitro* cellular uptake and cytotoxicity in EGFR-overexpressing breast cancer cells, compared to NT-BCMs (17,24). Therefore, we now report, the pharmacokinetics and biodistribution of the NT- and T-BCMs, as well as intratumoral distribution as determined by SPECT/CT and autoradiographic imaging (Fig. 1). In particular, the intratumoral distribution of NT- and T-BCM were mapped with respect to microvessel distribution and densities within the tumors. The tumors were also fractionated for quantification of BCMs (NT and T) in the extracellular matrix and intracellular compartment. This study demonstrates the use of multifunctional BCMs in combination with conventional and image-based methods to fully elucidate the whole-body and intratumoral transport of these systems *in vivo*.

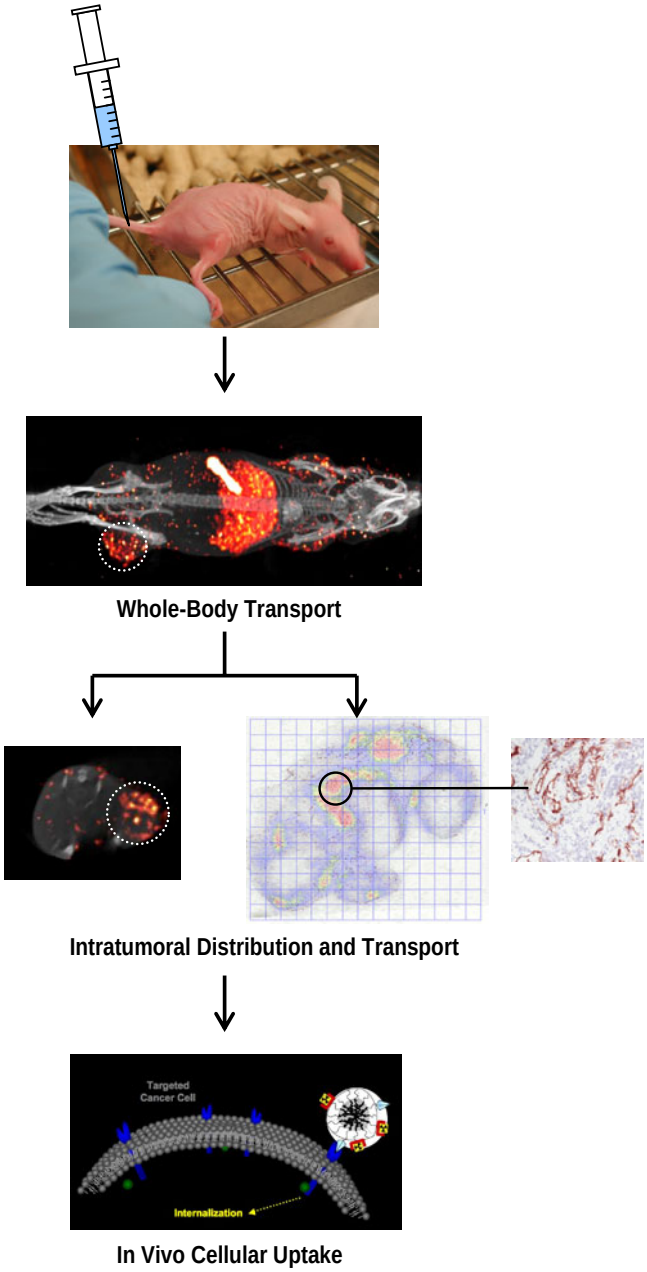

Fig. 1. Scheme outlining the scope of the current studies. Tumor-bearing mice were injected with ^{111}In-NT-BCMs or ^{111}In-T-BCMs. The whole-body transport of BCMs was studied via traditional pharmacokinetics and biodistribution studies. MicroSPECT/CT imaging also provided a qualitative assessment of the whole-body and intratumoral distribution of NT- and T-BCMs. The intratumoral distribution of BCMs was examined at a higher spatial resolution using autoradiographic imaging, which was mapped with respect to the intratumoral microvessel densities. Lastly, the *in vivo* cellular uptake of NT- and T-BCMs was quantified by disaggregating the tumors into extracellular and intracellular fractions.

MATERIALS AND METHODS

Materials

Methoxy poly(ethylene glycol) (MePEG, M_n=5,000, M_w/M_n=1.06) was purchased from Polymer Source Inc. (Montreal, QC, Canada). Heterobifunctional α-hydroxy-ω-amino poly(ethylene glycol) (HO-PEG-NH_2, M_n=5,000, M_w/M_n=1.08) and α-hydroxy-ω-carboxyl poly(ethylene glycol) (HO-PEG-COOH, M_n=4,910, M_w/M_n=1.05) were purchased from Jenkem Technology Inc. (Beijing, China). Dimethylsulfoxide (DMSO), hydrochloric acid (HCl in ether, 1.0 M), triethylamine, calcium hydride, human EGF, N-hydroxy succinimide, *N,N*-dimethylformamide (DMF), *N,N′*-dicyclohexyl carbodiimide (DCC) were purchased from Sigma-Aldrich (Oakville, ON, Canada). ^{111}In-chloride was obtained from MDS Nordion (Kanata, ON, Canada). 2-(4-isothiocyanatobenzyl)-diethylenetriaminepentaacetic acid (*p*-SCN-Bn-DTPA) was purchased from Macrocyclics Inc. (Dallas, TX). Toluene, dichloromethane, and ε-caprolactone (ε-CL) were purchased from Sigma-Aldrich (Oakville, ON, Canada), dried under calcium hydride and distilled prior to use. All chemicals were used as received unless otherwise specified.

Synthesis, Purification, and Characterization of Copolymers

MePEG-*b*-PCL, NH_2-PEG-*b*-PCL, and COOH-PEG-*b*-PCL copolymers were synthesized via metal-free cationic ring-opening polymerization of ε-CL using established methods described in detail elsewhere (25,26). Characterization, including ^{1}H NMR assignments for MePEG-*b*-PCL and NH_2-PEG-*b*-PCL, were published in a previous report (25). ^{1}H NMR assignments for COOH-PEG-*b*-PCL copolymers are as follows: δ=1.38 ppm (2H, CO-CH_2-CH_2-***CH_2***-CH_2-CH_2-O), 1.61 ppm (4H, CO-CH_2-***CH_2***-CH_2-***CH_2***-CH_2-O), 2.29 ppm (2H, CO-***CH_2***-CH_2-CH_2-CH_2-CH_2-O), 2.72 ppm (6H, -**CH_2**-S-***CH_2***-***CH_2***-COOH), 3.62 ppm (4H, -***CH_2***-***CH_2***-O), 4.04 ppm (2H, CO-CH_2-CH_2-CH_2-CH_2-C**H_2**-O) and 4.2 ppm (2H, O–CH_2–C**H_2**–O–CO). EGF-conjugated copolymers were prepared as previously reported by activating the COOH-PEG-*b*-PCL copolymers with NHS in the presence of DCC, with subsequent conjugation of EGF to the NHS terminus (17). EGF conjugation efficiency was found to be 42% using the Micro BCA Protein Assay (Pierce Inc.; Rockford, IL) with a standard curve prepared from known concentrations of EGF (26).

Radiolabeling of Copolymers

^{111}In-PEG-*b*-PCL copolymers were prepared as previously reported (25). Briefly, *p*-SCN-Bn-DTPA (2×mol excess, dissolved in DMSO) was conjugated to NH_2-PEG-*b*-PCL in 0.1 M sodium bicarbonate buffer (pH=8.5) for 4 h at room temperature. DTPA-PEG-*b*-PCL was purified using a size-exclusion column (Bio-Gel P2; BioRad, CA). ^{111}In was chelated to the DTPA-PEG-*b*-PCL copolymers in 0.1 M sodium acetate buffer (pH=6) for 30 min at 37°C immediately before use; the radiochemical purity of the copolymers was determined using instant thin-layer silica-gel chromatography (ITLC-SG; Pall Corp.) with development in 0.1 M sodium citrate buffer (pH=6). ^{111}In-PEG-*b*-PCL copolymers with radiochemical purity of ≥94% were used for all experiments.

Preparation and Characterization of ^{111}In-labeled NT-BCMs and T-BCMs

MePEG-*b*-PCL copolymers were dissolved in DMF and dried under nitrogen to form a dry copolymer film. The film was hydrated with phosphate-buffered saline (PBS) (pH=7.4, 0.01 M) at 60°C to form NT-BCMs (EGF-) at a concentration of 50 mg/mL. ^{111}In-PEG-*b*-PCL copolymers (<1 mol %) were added to the NT-BCMs, stirred for 1 h at 60°C and overnight at room temperature to allow for uniform distribution of the ^{111}In-PEG-*b*-PCL copolymers in the preformed NT-BCMs. For preparation of T-BCMs (EGF+), EGF-PEG-*b*-PCL copolymers (0.2 mol %; equivalent to approximately 1 EGF/micelle assuming an aggregation number of 500) were added along with the ^{111}In-PEG-*b*-PCL for copolymer transfer into the preformed NT-BCMs. The dissociation of ^{111}In from the BCMs and the transchelation of ^{111}In to transferrin under physiological conditions was found to be minimal as published in detail elsewhere (25).

The effective mean diameter and zeta potential of NT-BCMs and T-BCMs were measured using the 90 Plus Particle Size Analyzer (Brookhaven Instruments Corp., NY). The BCMs were chelated with non-radioactive $InCl_3$ (purity >98%; Sigma-Aldrich, Oakville) and were diluted to a concentration of 1 mg/mL prior to measurements.

Tumor Inoculation

Balb/C female athymic mice of 4–6 weeks of age (16–20 g) were used for tumor inoculation. The mice were housed 5 per cage under standard conditions with access to food and water *ad libitum*. Mice were inoculated in the right flank subcutaneously with 1×10^7 MDA-MB-468 cells (10^6 EGFR/cell, EGFR-overexpressing tumor) suspended in DMEM (10% fetal bovine serum, 1% penicillin-streptomycin). For MCF-7 tumor-bearing mice (10^4 EGFR/cell), the mice were implanted intradermally with a 17-β-estradiol pellet (Innovative Research of America; Sarasoto, Florida) at least 24 h prior to inoculation with 2×10^7 cells subcutaneously. Animal studies were conducted under a protocol approved by the Animal Care Committee at the University Health Network (AUP 989.3) and following Canadian Council on Animal Care guidelines.

In Vivo Pharmacokinetics and Biodistribution Studies

Tumors were allowed to grow until reaching a diameter of 4–8 mm (2–3 weeks post-inoculation) for *in vivo* pharmacokinetics and biodistribution studies. Mice were injected intravenously via the tail vein with BCMs (250 mg of copolymer/kg, 3-4 MBq/mouse). At 5 min, 15 min, 30 min, 1, 2, 4, 8, 12, 24, 48, and 72 h post-injection (h.p.i.), blood samples were collected from the saphenous vein using a heparinized capillary tube. For biodistribution studies, the animals were anesthetized and sacrificed by cardiac puncture. Tissue samples, including heart, lung, liver, kidneys, spleen, and tumor, were collected at 4, 24, 48, and 72 h.p.i.. The amounts of radioactivity in the blood and tissue samples were determined by γ-counting.

MicroSPECT/CT Imaging

MicroSPECT/CT imaging was used as a non-invasive tool to image the tissue deposition of ^{111}In-BCMs in the MDA-MB-468 tumor-bearing mice (25). Each mouse was injected with 37 MBq of ^{111}In-BCMs (250 mg/kg) via tail-vein injection. MicroSPECT/CT images were acquired at 48 h post-injection using a NanoSPECT/CT small animal tomograph (Bioscan, Washington, DC). Cone-beam CT scans were performed prior to helical SPECT image acquisition (minimum of 100,000 counts per projection). InvivoScope image processing software (Bioscan, version 1.34) was used for reconstruction and coregistration of the SPECT/CT images.

Intratumoral Distribution of ^{111}In-NT-BCMs and ^{111}In-T-BCMs

Immediately following γ-counting, excised tumors (collected at 48 h.p.i.) were placed into a cryomold containing

Tissue-Tek® O.C.T. compound (Electron Microscopy Sciences; Hatfield, PA). The tumors were frozen in an isopentane bath in liquid nitrogen for 10 s. The tumor samples were then cut into 8 μm thick sections. Histology staining including anti-CD-31 antibody (for visualization of blood vessels), as well as hematoxylin and eosin (H&E), was performed (Pathology Research Program, University Health Network) on consecutive tissue sections immediately next to the tumor section used for autoradiography.

One week following tumor excision, the unstained tumor sections were exposed to a MultiSensitive Screen (PerkinElmer Inc., MA) in an autoradiography cassette for 72 h. The autoradiographic image was recorded using the Cyclone® Plus Storage Phosphor System (PerkinElmer Inc., MA). The intratumoral distribution of ^{111}In-BCM was analyzed by quantifying the amount of radioactivity within the tumor sections using the OptiQuant™ Image Analysis Software (PerkinElmer Inc., MA). The autoradiographic image was overlaid with the CD-31-stained section using Adobe® Photoshop (version 10.0.1). A grid of regions of interest (ROI) with equal areas of 0.5 by 0.5 mm was arbitrarily assigned to each autoradiographic image and the corresponding overlaid CD-31-stained image. The amounts of radioactivity on the autoradiographic image were presented as digital light units (DLU). The total blood vessel area (expressed in pixels) in each of the 0.5×0.5 mm grids was measured using a customized image analysis program written in MATLAB® (version 7.5.0.342, R2007b). Pearson correlation and linear regression analyses were used to evaluate the correlation between DLU and the total blood vessel area within the corresponding regions within each tumor section.

In Vivo Cellular Uptake of ^{111}In-BCMs in Tumors

The *in vivo* cellular uptake of ^{111}In-BCMs was determined following an optimized protocol that was previously published by our group with slight modifications (27,28). Briefly, tumor samples collected from biodistribution studies at 4, 24, 48, and 72 h.p.i. were thoroughly minced with a scalpel and were transferred to a 5 mL polypropylene tube containing 0.3 mL of a 0.2 M sodium acetate buffer (pH=2.5). The tissue samples were disaggregated using a Sonic Dismembrator-Model 100 (Fisher Scientific, Pittsburg, PA). A 2.2 mL aliquot of the acetate buffer was added to each of the homogenized samples, followed by a 10 min incubation on ice. Extracellular and membrane-bound radioactivity (supernatant) were separated from the cells after centrifugation at 6,311×g for 10 min, followed by two PBS rinses. The radioactivity in the final cell pellet (intracellular fraction) and the extracellular/membrane bound fraction were measured by γ-counting. This method was validated previously and was shown to result in highly pure cytoplasmic fractions (27,28). Homogenization of the tissue samples likely leads to a certain degree of cell rupture; therefore, the amount of ^{111}In-BCMs measured in the intracellular fractions may be an underestimate. However, it should be noted that all tumors harvested from each treatment group (both xenografts injected with NT-BCMs or T-BCMs) were disaggregated in the same manner. In this way, the data afforded a relative comparison between treatment groups with no preferential bias towards mice treated with either NT-BCMs or T-BCMs.

Statistical Analyses

All results were obtained from groups of $n \geq 3$ and are expressed as mean ± standard deviation (SD). Statistical analyses were performed using SPSS (Statistical Package for the Social Sciences, version 14.0). Two-sample *t*-test was used to measure statistical significance between pairs of results, and $p<0.05$ was considered to be significant. For statistical analyses among three or more groups, one-way analysis of variance (ANOVA) was used, and subsequent multiple comparisons with Bonferroni correction were performed if the ANOVA *F*-test detected any statistical significance. Pearson correlation and linear regression analyses were used for analyzing data from the autoradiography studies.

RESULTS

Characterization of In-NT-BCMs and In-T-BCMs

NT- and T-BCMs prepared mainly from PEG_{5000}-*b*-PCL_{5000} copolymers were found to have effective mean diameters of 57±8 nm and 61±1 nm, respectively. Previous studies demonstrated that the NT-BCMs were stable and maintained their size for at least 6 days in the presence of physiological concentrations of the protein albumin (45 g/L) (25). The zeta potentials of the NT- and T-BCMs were −6.4 mV and −7.3 mV, respectively. Overall, the conjugation of EGF as a targeting moiety on T-BCMs has a negligible effect on the physico-chemical properties of the BCMs.

Pharmacokinetics of ^{111}In-NT-BCMs and ^{111}In-T-BCMs

Fig. 2 presents the pharmacokinetics profiles of NT-BCMs (EGF-) and T-BCMs (EGF+) evaluated in two tumor-models, MDA-MB-468 (10^6 EGFR/cell, EGFR-overexpressing) and MCF-7 (10^4 EGFR/cell, low level of EGFR expression). Both NT- and T-BCMs were found to exhibit biphasic pharmacokinetics profiles, with no significant difference observed between the treatment groups. The data were fit using a two-compartment model with the assumption of elimination from the central compartment (25,29). Table I presents the pharmacokinetics parameters obtained by fitting the data using mathematical modeling software (Scientist version 2.01, Micromath®; Saint Louis, Missouri). The pharmacokinetics parameters obtained in the two xenograft models were comparable with the exception of the area under the curve (AUC_{plasma}) and volume of distribution (V_{dss}). The AUC_{plasma} and V_{dss} of NT-BCMs in the MCF-7 tumor-bearing mice were 25% lower ($p<0.001$) and 65% higher ($p=0.038$) than in the MDA-MB-468 tumor-bearing mice, respectively. Importantly, the total clearance (CL_{total}) of T-BCMs was statistically similar to that of the NT-BCMs in both tumor models ($p=0.227$). Overall, the conjugation of EGF to BCMs (T-BCMs) did not alter their *in vivo* distribution and elimination kinetics.

Biodistribution and Tumor Accumulation Kinetics of ^{111}In-NT-BCMs and ^{111}In-T-BCMs

The tissue uptake kinetics of BCMs (NT-BCMs and T-BCMs) in MDA-MB-468 and MCF-7 tumor-bearing mice are presented in Tables II and III. In the case of MDA-MB-468

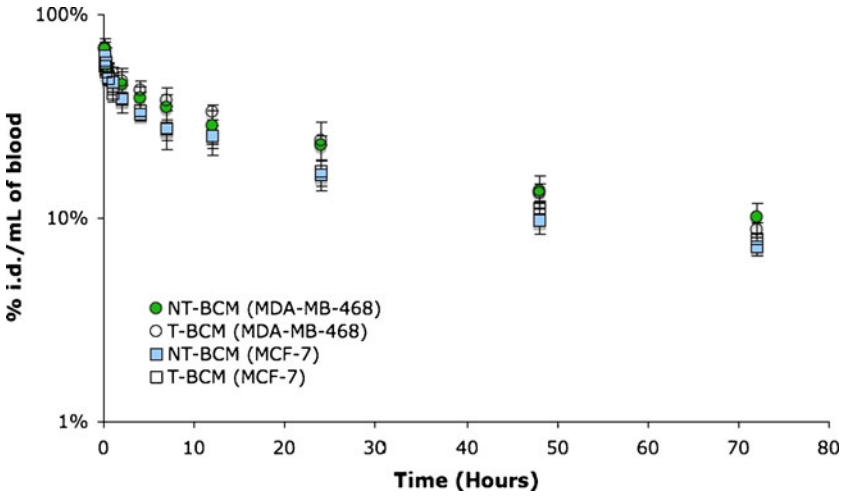

Fig. 2. Pharmacokinetic profiles of the NT- and T-BCMs labeled with ^{111}In, in MDA-MB-468 and MCF-7 tumor-bearing mice. The mice were injected intravenously at a dose of 250 mg/kg of PEG-*b*-PCL copolymer. Blood concentrations of BCMs were expressed as percentage of injected dose/mL of blood (% i.d./mL of blood) and were corrected for decay.

tumor-bearing mice, most of the tissue uptake of BCMs was highest at 4 h.p.i. Beyond 24 h.p.i., minimal uptake of BCMs (<5% i.d./g) was found in organs such as heart, lung, and kidneys, for both tumor models. As expected, BCM accumulation was highest in the liver and spleen (9–30% i.d./g). No significant difference was detected between the accumulation of NT-BCMs and T-BCMs in tissues when comparison was made within the same tumor model ($p>0.1$).

Fig. 3 represents the total accumulation kinetics of NT- and T-BCMs in MDA-MB-468 and MCF-7 tumors. There was no significant difference detected between the tumor deposition of NT-BCMs and T-BCMs in the MCF-7 tumors at all time points ($p>0.223$), suggesting that the T-BCMs do not preferentially accumulate in tissues expressing low levels of EGFR (10^4 EGFR/cell). For the EGFR-overexpressing MDA-MB-468 tumor model (10^6 EGFR/cell), the T-BCMs led to a marginal but statistically significant increase in tumor accumulation ($p=0.021$ for 4 h.p.i.; $p=0.05$ for 24 h.p.i.; $p=0.022$ for 48 h.p.i.; $p=0.006$ for 72 h.p.i.).

MicroSPECT/CT Imaging in Mice Bearing MDA-MB-468 Tumors

MicroSPECT/CT imaging was performed at 48 h.p.i. to provide a qualitative assessment of the tissue deposition of NT-BCMs and T-BCMs in the MDA-MB-468 tumor-bearing mice (Fig. 4). In agreement with the biodistribution data (Tables II & III), the liver and spleen were found to contain a substantial amount of both NT-BCMs and T-BCMs in the maximum intensity projection images. The intratumoral distribution of NT-BCMs and T-BCMs was examined via the transversal view at the tumor region (4 mm/image). In general, the intratumoral distribution of BCMs was found to be heterogeneous, with regions of high radioactivity seen mostly at the tumor periphery. This is in agreement with previously published observations by our group (25).

Intratumoral Distribution of ^{111}In-NT-BCMs and ^{111}In-T-BCMs

Fig. 5a and b include representative autoradiographic images outlining the distribution of NT-BCMs and T-BCMs, respectively, within the MDA-MB-468 tumors. In general, the distribution of both NT-BCMs and T-BCMs were very heterogeneous, with some regions within the tumors showing only background radioactivity. However, it can be seen that areas with high amounts of radioactivity are mostly associated with intense CD-31-staining (endothelial cells stained in brown) as illustrated in Fig. 5. Similar intratumoral distribu-

Table I. Summary of Pharmacokinetic Parameters

	MDA-MB-468 xenograft		MCF-7 xenograft	
Parameters	NT-BCMs	T-BCMs	NT-BCMs	T-BCMs
$t_{1/2,\alpha}(h)$	0.4±0.2	0.4±0.2	0.7±0.4	0.7±0.4
$t_{1/2,\beta}(h)$	29±4	30±3	31±3	33±5
V_1 (mL)	1.3±0.3	1.4±0.2	1.6±0.2	* 1.8±0.1
V_{dss} (mL)	2.0±0.1	2.08±0.09	* 3.1±0.4	* 3.1±0.6
CL_{total} (mL/h)	0.06±0.02	0.05±0.01	0.07±0.01	0.065±0.005
AUC_{total} (%i.d.•h/L)	2,000±400	1,900±200	1,500±200	* 1,500±100

Mathematical modeling was performed using the Scientist software (Micromath®). Data were fit using a two-compartment model with an i.v. bolus injection, assuming clearance from the central compartment.
*$p<0.05$ when compared to MDA-MB-468 xenograft. No statistical significant difference was detected between treatment groups.

Table II. Tissue Uptake of ^{111}In-NT-BCMs and ^{111}In-T-BCMs in Athymic Mice Bearing Subcutaneous Breast Cancer Xenografts Overexpressing EGFR (MDA-MB-468 Tumors, 10^6 EGFR/Cell)

		Percentage of injected dose / gram of organ (mean ± SD)				
Treatment	Time (h.p.i.)	Heart	Kidneys	Lung	Liver	Spleen
NT-BCMs	4	1.6±0.4	4.1±0.2	3.6±0.5	8.0±1.0	21.9±0.7
	24	0.7±0.2	2.3±0.3	1.2±0.4	12.1±1.7	23.9±0.3
	48	0.4±0.1	1.9±0.8	0.7±0.3	11.2±3.6	10.8±1.0
	72	0.7±0.2	1.9±0.7	0.6±0.2	10.6±2.9	9.4±3.5
T-BCMs	4	1.4±0.4	4.7±0.4	3.0±1.1	9.5±0.7	27.0±8.8
	24	0.9±0.2	2.7±0.5	1.5±0.4	* 9.2±1.0	25.2±5.3
	48	* 0.7±0.2	2.1±0.5	* 1.1±0.3	9.6±2.0	11.2±3.1
	72	0.6±0.4	2.0±0.6	0.7±0.2	8.9±1.2	10.6±5.3

*$p<0.05$ when compared between treatment groups for the MDA-MB-468 xenografts.

tions of NT- and T-BCMs were also observed in MCF-7 tumor-bearing mice (data not shown).

In order to quantify the correlation between localization of BCMs and tumor blood vessels, Pearson correlation analyses of the amounts of radioactivity and the blood vessel densities within regions of interest (ROI) were performed. Examples of the correlation analyses are presented in Fig. 5a and b. Multiple tumors ($n\geq4$) in each treatment group were used, and these data are presented in Table IV. The intratumoral distribution of both NT- and T-BCMs were positively correlated with the blood vessel densities ($p<0.001$) with r values ranging from 0.68±0.04 to 0.70±0.07. These results quantitatively support the previous observation made from Fig. 5: regions within the tumor with higher blood vessel densities are likely to accumulate more BCMs. In addition, it was found that the attachment of EGF as a targeting moiety did not influence the intratumoral distribution of BCMs, since no significant difference in the correlation coefficients was observed ($p>0.96$).

In Vivo Cellular Uptake of ^{111}In-NT-BCMs and ^{111}In-T-BCMs

Fig. 6a and b show the amounts of radioactivity in the intracellular and extracellular compartments, respectively, in the MDA-MB-468 and MCF-7 tumors at multiple time points. For the MCF-7 tumor-bearing mice, the amounts of intracellular NT-BCMs and T-BCMs increased from approximately 2,200 pmol/g to 5,000 pmol/g from 4 to 72 h.p.i.. The intracellular NT-BCMs and T-BCMs detected in the MCF-7 tumors were statistically similar ($p>0.425$), indicating that receptor-ligand endocytosis does not significantly increase *in vivo* cellular uptake in tumors expressing a low level of EGFR.

For the MDA-MB-468 tumors, the amount of cell-internalized radioactivity was found to decrease over time in groups of mice injected with NT-BCMs or T-BCMs ($p<0.05$). The ratios of intracellular T-BCMs to NT-BCMs were 1.9 ($p=0.028$), 2.2 ($p<0.01$), 1.9 ($p=0.037$), 2.3 ($p=0.007$) at 4, 24, 48, 72 h.p.i., respectively. The intracellular BCM content measured may also include uptake by the tumor-associated macrophages (TAM). Since TAM do not express EGFR on their cell surface (30), it is believed that TAM uptake did not play a role in the enhanced cell uptake of T-BCM in the MDA-MB-468 tumors. Up to 90% and 70% of the total radioactivity accumulating in the tumor was detected in the extracellular tumor interstitium for the MDA-MB-468 and MCF-7 tumors, respectively. A portion of the measured extracellular radioactivity may be attributed to the cell membrane-bound copolymer since an acidic solvent (sodium acetate buffer, pH=2.5) and mechanical force (homogenization) were used while disaggregating the tumors. The higher

Table III. Tissue Uptake of ^{111}In-NT-BCMs and ^{111}In-T-BCMs in Athymic Mice Bearing Subcutaneous Breast Cancer Xenografts Expressing Low Levels of EGFR (MCF-7 Tumors, 10^4 EGFR/Cell)

		Percentage of injected dose / gram of organ (mean ± SD)				
Treatment	Time (h.p.i.)	Heart	Kidneys	Lung	Liver	Spleen
NT-BCMs	4	§ 0.3±0.1	§ 2.5±0.2	§ 1.2±0.6	§ 32.0±2.3	17.7±9.7
	24	0.4±0.4	2.1±0.6	0.9±0.5	§ 30.3±4.3	14.4±7.2
	48	0.2±0.1	1.7±0.5	0.4±0.0	14.9±6.1	13.4±4.2
	72	0.4±0.3	1.2±0.6	0.3±0.2	11.8±5.5	7.4±3.9
T-BCMs	4	§ 0.2±0.1	§ 2.3±0.7	§ 0.9±0.5	§ 32.1±3.6	14.3±5.6
	24	§ 0.2±0.0	2.1±0.3	0.7±0.6	19.9±8.9	13.4±7.6
	48	§ 0.2±0.1	1.4±0.2	§ 0.4±0.1	14.2±5.6	12.5±3.5
	72	0.7±0.4	1.5±0.3	0.6±0.5	9.6±2.2	10.1±5.4

§ $p<0.05$ when compared to MDA-MB-468 xenograft. No statistical significant difference was detected between treatment groups.

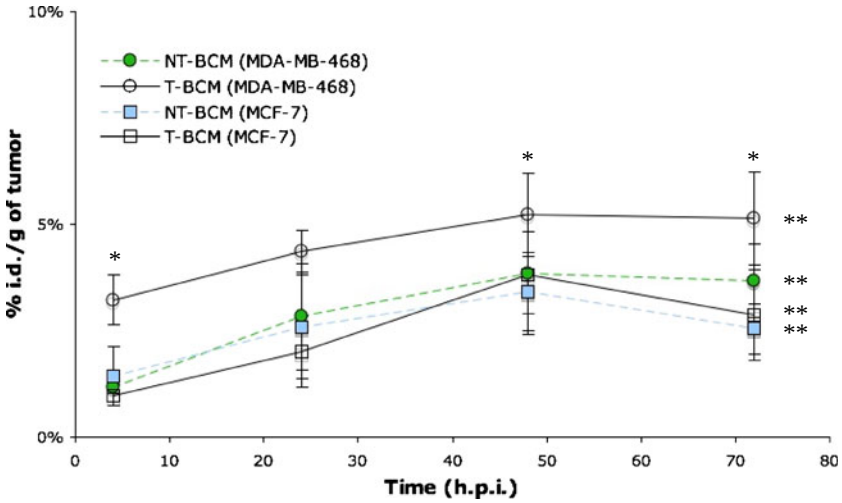

Fig. 3. Tumor accumulation kinetics of the NT- and T-BCMs labeled with ^{111}In, in MDA-MB-468 and MCF-7 tumor-bearing mice that were injected intravenously at a dose of 250 mg/kg of PEG-*b*-PCL copolymer. The amounts of BCM accumulated in the tumors were expressed as percentage of injected dose per gram of organ and were corrected for decay. * $p<0.05$ for comparison between T-BCMs and NT-BCMs for the MDA-MB-468 xenografts. ** $p<0.05$ for data obtained at 4 and 72 h.p.i. within the same treatment group.

extracellular accumulation of T-BCMs in the MDA-MB-468 tumors is likely a result of their enhanced affinity towards the overexpressed EGFR on the MDA-MB-468 tumor cells. The same observation was obtained *in vitro* where T-BCMs increased the fraction of cell membrane-bound micelles in the MDA-MB-468 cells ($p=0.0002$), but not in the MCF-7 cells ($p=0.253$) (data not shown).

DISCUSSION

Physico-chemical Properties of BCMs and their Whole-Body Transport

The physico-chemical properties of NDDS play a significant role in their whole-body transport. It is well accepted that an

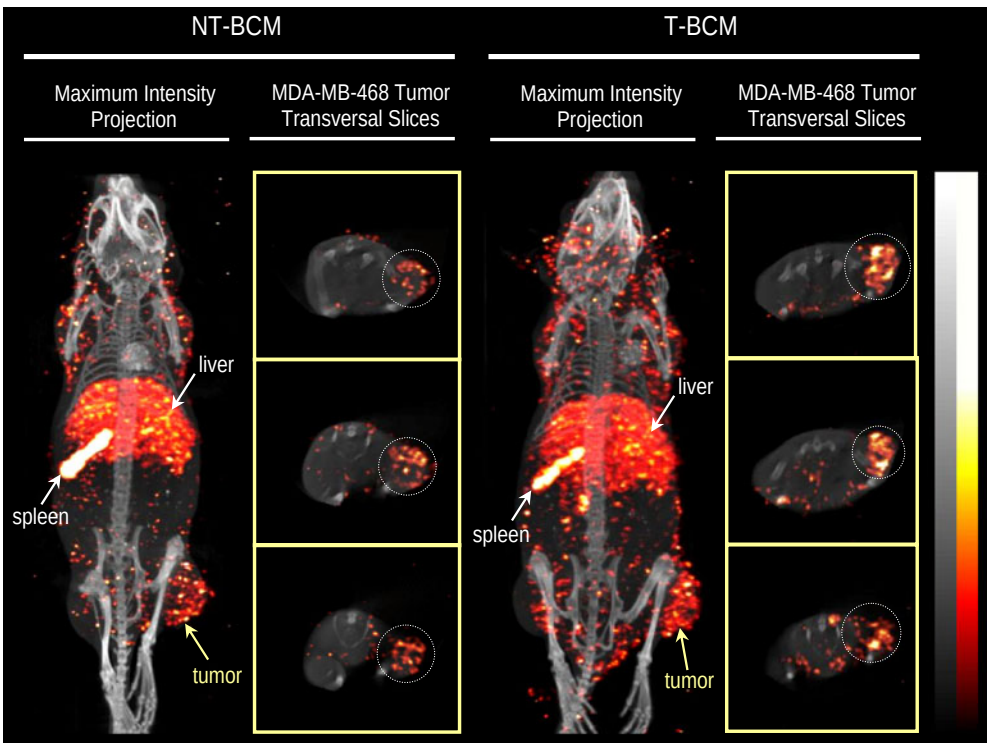

Fig. 4. MicroSPECT/CT images illustrating the whole-body transport of the NT- and T-BCMs labeled with ^{111}In, in MDA-MB-468 tumor-bearing mice that were injected intravenously at a dose of 250 mg/kg of PEG-*b*-PCL copolymer. The maximum intensity projection and the tumor transverse slice images were acquired at 48 h.p.i.. The tumor transverse slices shown represent consecutive sections of the tumor at an approximate thickness of 4 mm/section.

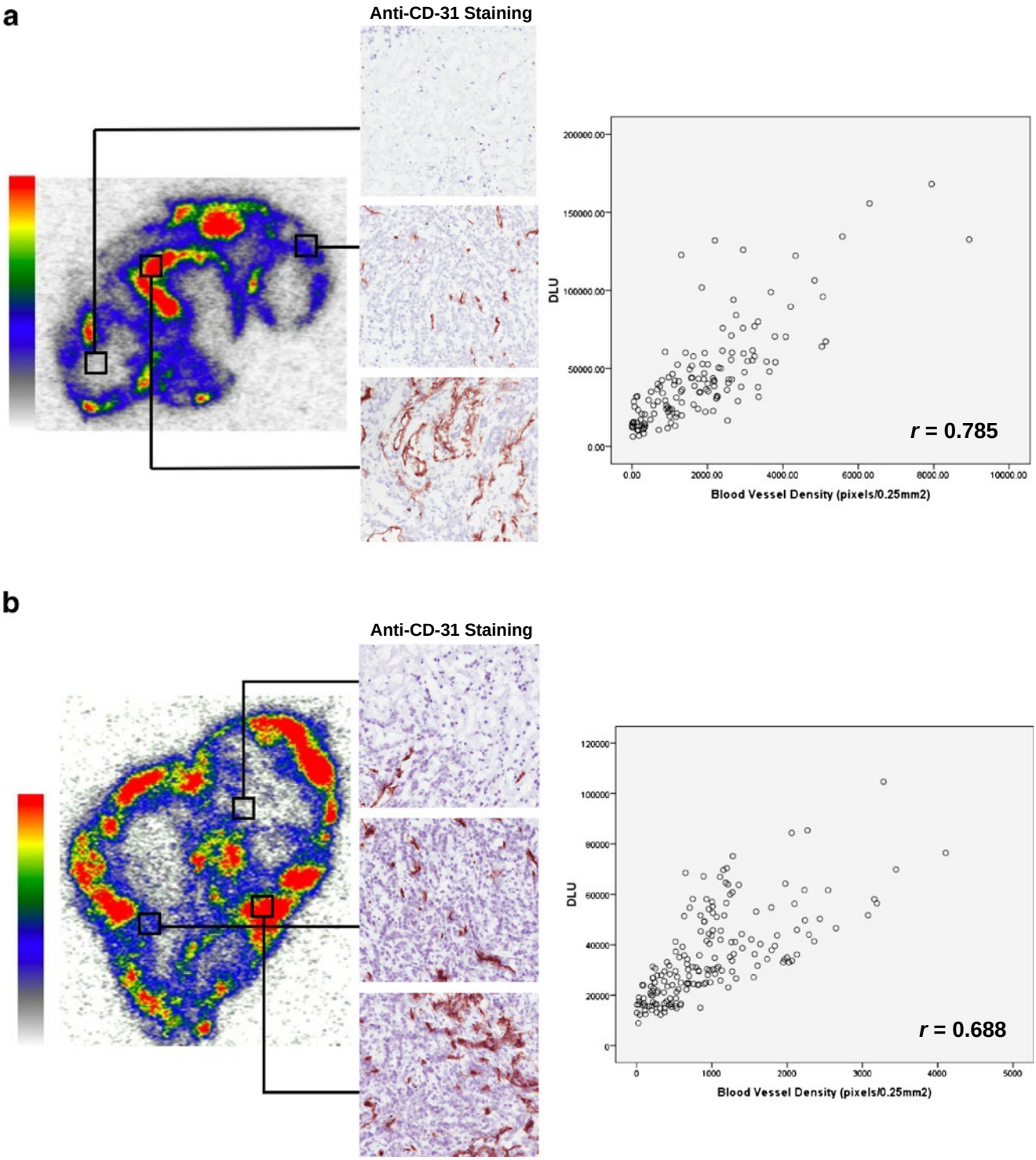

Fig. 5. Intratumoral distribution of (**a**) ^{111}In-NT-BCMs and (**b**) ^{111}In-T-BCMs obtained in MDA-MB-468 tumor-bearing mice at 48 h post-injection. Tumors were cut into 8 μm thick sections for autoradiographic imaging. Consecutive tumor sections were stained with anti-CD-31 antibody for visualization of tumor blood vessels (in brown). An overlay of the autoradiography and the anti-CD-31 antibody stained images is presented on the left. The amount of radioactivity on the autoradiography image is represented by the coloured scale bar and is quantified as digital light units (DLU). Pearson correlation analyses of DLU and blood vessel density (CD-31 positive) are presented on the right.

extended circulation half-life is key to achieving therapeutically relevant levels of NDDS tumor deposition via the EPR effect (6,31). The extended circulation half-lives ($t_{1/2,\beta} > 29 \pm 4h$) of the BCMs reported here are attributed to their hydrophilic PEG-shell, as well as their favorable thermodynamic and kinetic stability (29). The high level of BCM uptake detected in organs such as liver (8–32.1% i.d./g) and spleen (7.4–27% i.d./g) is attributed to the role of these organs in the clearance of foreign particulates as components of the mononuclear phagocytic system (32). These values were found to be comparable to other long-circulating BCM systems reported elsewhere (5,25,29).

Table IV. Pearson Correlation Coefficients for Radioactivity (Digital Light Unit) and Blood Vessel Density (CD-31 Positive) in Tumors Sampled from MDA-MB-468 and MCF-7 Tumor-Bearing Mice 48 h Post-injection with ^{111}In-NT-BCMs or ^{111}In-T-BCMs

Correlation coefficients (radioactivity *vs*. blood vessel density)		
Tumor model	NT-BCMs	T-BCMs
MDA-MB-468	0.70±0.07	0.69±0.05
MCF-7	0.70±0.1	0.68±0.04

It has been reported that functionalizing the NDDS surface with certain targeting moieties can accelerate plasma clearance and increase tissue uptake (5,15). For instance, Bae *et al.* found that a 10-fold increase in folate content on the surface of BCMs resulted in more than a 2-fold increase in liver uptake, which is attributed to the recognition of the folate ligand by liver cells and/or opsonization by plasma folate binding proteins (5). In the current study, the pharmacokinetics (Fig. 2 & Table I) and the tissue uptake (Tables II & III) of NT-BCMs and T-BCMs were proven to be similar. The lack of increased T-BCM uptake in the liver or kidneys ($p>0.1$) indicates that the conjugation of EGF to the BCMs did not increase their affinity towards organs expressing intermediate levels of EGFR (10^5 EGFR/cell in liver and kidneys) (33,34). A previous study by our group demonstrated that T-BCMs (EGF+) exhibit lower binding affinity towards EGFR than the endogenous EGF molecules (35), which could contribute to the observation that EGF conjugation had negligible effects on the pharmacokinetics and tissue uptake of these particles.

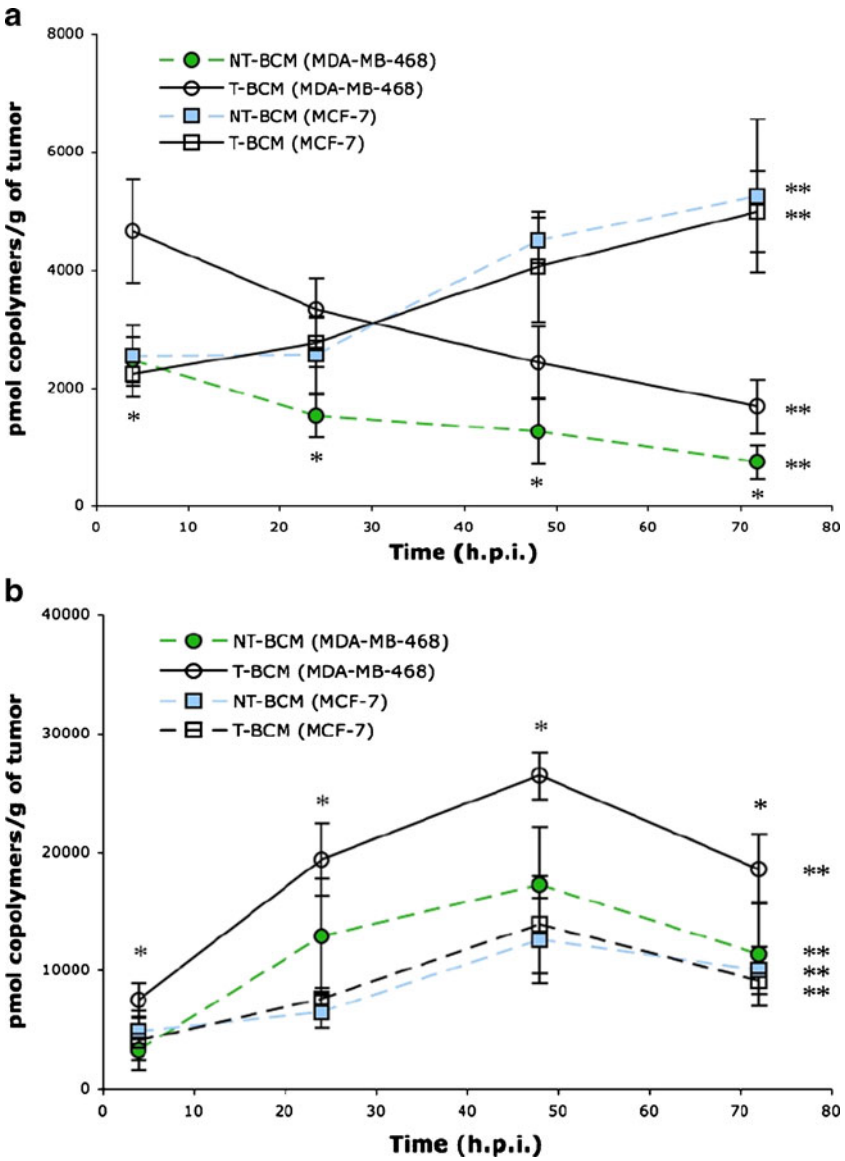

Fig. 6. Amount of PEG_{5000}-*b*-PCL_{5000} copolymer measured in the (**a**) intracellular and (**b**) extracellular compartments in the MDA-MB-468 and MCF-7 tumors following tissue fractionation. The amount of uptake is presented as pmol of copolymer/g of tumor. * $p<0.05$ for comparison between T-BCMs and NT-BCMs for the MDA-MB-468 xenografts. ** $p<0.05$ for data obtained at 4 and 72 h.p.i. within the same treatment group.

Impact of Tumor Physiology on Passive Targeting and Intratumoral Distribution of BCMs

Traditionally, the study of BCM biodistribution in murine tumor models involves harvesting the organs of interest and subsequently quantifying the BCM-encapsulated drugs and/or the radiolabeled polymers within the organs. This technique allows only for assessment of drugs and/or BCM accumulation in the entire organ, but provides no information on their distribution within the tissue. Advances in imaging methods have afforded effective ways to study the transport and microdistribution of BCMs with improved spatial resolution. In the current study, we observed a highly heterogeneous distribution and incomplete penetration of NT- and T-BCMs in the tumors using microSPECT/CT and autoradiographic imaging. Histological and autoradiographic analyses confirmed that the presence of more and/or larger blood vessels facilitated the transvascular transport of BCMs into the tumor interstitium. These results imply that BCM formulations may be more efficacious in tumors with a high degree of vascularization and less effective in treating hypovascular tumors due to their inability to fully exploit the EPR effect.

It should be noted that the extent of tumor vascularization is not the only physiological factor affecting passive targeting and the intratumoral distribution of BCMs. Other physiological factors such as vascular permeability, interstitial fluid pressure (IFP), and extracellular matrix components also play significant roles in the transport of BCMs in the tumor interstitium (3,31,36). Vascular permeability in hyperpermeable blood vessels can vary greatly within a tumor and/or in different tumor models, with endothelial fenestrations ranging from 200 nm to 4.7 μm (3,36,37). In our previous study, it was found that the peak tumor accumulation of NT-BCMs at 48 h. In MDA-MB-231 breast cancer xenografts, p.i. was 9±2% i.d./g (25). This value is approximately 2-fold higher than the total tumor accumulation of NT-BCMs obtained in the current study (Fig. 3). The MDA-MB-231 tumors may possess a more permeable vascular network than the MDA-MB-468 and MCF-7 tumors, resulting in an increased transvascular transport of BCMs. Similarly, McLarty *et al.* also reported a 3.2-fold increase in the tumor accumulation of the non-specific control ^{111}In-DTPA-mIgG (i.e. accumulation via EPR) in the MDA-MB-231 xenografts compared to the MCF-7 xenografts (38).

A consequence of hyperpermeable tumor vasculature development is an elevated IFP in the tumor interior compared to the tumor periphery. The periphery of a tumor is usually more hypervascular, while the center of the tumor tends to be less vascularized and sometimes necrotic (39). Elevated IFP in the tumor is attributed to increased fluid and plasma protein transport into the tumor interstitial space, coupled with poor lymphatic drainage (36,40). As a result, extravasated BCMs are likely to be directed towards the tumor periphery via convective flow. The intratumoral distribution of BCMs observed in the MDA-MB-231, MDA-MB-468, and MCF-7 tumors are in agreement with this theory, and as such, more "hot spots" of BCMs can be found in the periphery of the tumors (Fig. 4) (25,36). Indeed, this elevated IFP severely limits BCM penetration from the vascular surface into other regions within the tumor. Limited tumor penetration may reduce the exposure of T-BCMs to their target cells, impeding specific cell uptake of T-BCMs, which in turn becomes a possible barrier for active targeting.

In Vivo Cellular Uptake of BCMs and Active Targeting

The goal of pursuing active targeting in drug delivery is to achieve an enhanced intracellular content of the drug-loaded T-NDDS in order to increase the bioavailability of the drug at the tumor site. Therefore, successful active targeting does not necessarily require an enhancement in tumor deposition of the T-NDDS. For instance, Kirpotin *et al.* observed a 6-fold increase in the tumor cell uptake of anti-HER2-liposomes, yet the total tumor accumulation of the T- and NT-liposomes were equivalent (9). Nevertheless, others have shown that active targeting of NDDS can result in an enhancement in total tumor accumulation, without demonstrating if the T-NDDS leads to increased *in vivo* cellular uptake (11,41).

In the current study, a marginal increase in the tumor accumulation of T-BCMs was detected, along with enhanced *in vivo* intracellular and extracellular (cell binding + interstitial) uptake (Fig. 6). After the BCMs extravasated into the tumor interstitial space, nearby tumor cells can internalize the NT- and T-BCMs via non-specific and/or specific uptake. Due to limited tumor penetration, only a small portion of tumor cells located immediately next to the hyperpermeable vessels were capable of interacting with the BCMs. In this way, the cell uptake of BCMs in the tumors is quickly saturated, leaving the majority of BCMs in the interstitial space remaining non-cell-associated (<30% detected as intracellular). Elevated IFP in the tumors can lead to clearance of the non-cell-associated BCMs back to the circulation. In addition, TAM that engulf the nearby BCMs can eliminate these foreign particles. Therefore, it is plausible that the increased *in vivo* specific cellular uptake ($p<0.05$) and cell membrane binding ($p<0.043$) observed for the T-BCMs enhances their retention within the MDA-MB-468 tumors. Such receptor-ligand interactions between the EGFR on tumor cells and T-BCMs can delay their clearance from the tumors, elevating the tumor accumulation of T-BCMs in comparison to NT-BCMs. This hypothesized receptor-ligand interaction is supported by the fact that no significant difference was detected between the fractions of intracellular and extracellular NT- and T-BCMs at all time points in the MCF-7 tumors ($p>0.239$).

Although the ratios of intracellular T-BCM/NT-BCM remain constant in the MDA-MB-468 tumors, the intracellular content of both populations of BCMs was found to decrease significantly over time ($p<0.05$). This particular BCM efflux from cells is tumor-model specific and is independent of the mode of internalization (i.e. specific *vs*. non-specific). *In vitro*, it has been shown that exocytosis of BCMs can occur through the recycling of the endosomal compartments, following removal of the BCM-containing extracellular medium (42,43). However, *in vivo* exocytosis is different from *in vitro*, as the extracellular space in the tumors is saturated with BCMs following passive targeting. It is postulated that tumor-released exosomes may play a role in the efflux of BCMs in the MDA-MB-468 tumors. Tumor-released exosomes are known as sub-micron vesicles that originate from endosomes and can release intracellular content as a form of intercellular communication (44). The internalized BCMs may cross paths with the biogenesis of the endosomal-derived exosomes, as BCMs are known to accumulate in the endosomes following non-specific and specific

internalization (43,45). These internalized BCMs are then released to the extracellular space via transport in exosomes. Although internalization is a continuing process, a net efflux of BCMs can be observed if the rate of exocytosis exceeds that of the internalization kinetics. Panyam *et al.* suggested that BCMs accumulating in recycling endosomes are likely to have a fast turnover rate (43) and can result in rapid recycling of the internalized BCMs to the extracellular space. Although it is expected that T-BCMs experience more efficient internalization kinetics via receptor-ligand endocytosis, it seems that the rate at which these exosomes are released still overpowers the influx of T-BCMs. Interestingly, this unexpected efflux of BCMs was not observed in the MCF-7 tumors. However, the two different cell types may process BCMs in very distinct manners (46). For instance, tumor-released exosomes have been shown to play a role in stromal remodeling and promote the epigenetic transfer of metastatic activity *in vivo* (47). It has been established that breast cancers overexpressing EGFR (>10^4 EGFR/cell) are associated with more aggressive metastatic disease in cancer patients, although the MDA-MB-468 cell line is not known to be metastatic in athymic mice (48). It is likely that the ratio of exosome release/internalization kinetics in the MDA-MB-468 tumors (10^6 EGFR/cell) *in vivo* exceeds that in the MCF-7 tumors (10^4 EGFR/cell). As a result of the distinct kinetic rates of exocytosis/internalization, a net BCM efflux and influx is observed in the MDA-MB-468 and MCF-7 tumors, respectively.

The significant variability in BCM behaviour in the two breast cancer xenograft models illustrates that tumor physiology plays a significant role in their transvascular and intratumoral transport. Tumor physiology is known to be modulated according to the host environment, such as stromal-epithelial cell interactions, as well as presence of endogeneous and paracrine signaling factors in the extracellular matrix (49,50). Therefore, one must not attempt to generalize and extrapolate observations obtained from one murine tumor model to another and/or to humans, as tumor physiology can be extremely heterogenous across different species. However, the tumor microenvironment and disease progression in orthotopic tumor models are considered to be more representative of human disease than subcutaneous xenograft models in animals and are likely to produce more clinically relevant results. It should also be noted that understanding BCM transport *in vivo* does not necessarily represent the true fate of the drug content, as drug release rates vary extensively for each formulation and can therefore vastly alter the intratumoral localization of the drug. However, the information obtained in this study should provide useful insight for BCM systems with good drug retention. As discussed previously, at least 70% of the BCMs were located in the extracellular compartment following extravasation into the tumor interstitium. In order to fully exploit the therapeutic potential of BCMs localized in the extravascular space, the systems may be designed to release their drug content by means of thermal activation or ultrasonication at the tumor site (51,52). Triggering drug release in the extracellular space not only increases drug exposure to the tumor cells, but also promotes drug penetration within solid tumors. High molecular weight NDDS, such as liposomes and BCMs, have limited tumor penetration due to their low diffusion coefficient in the tumor interstitium; however, low molecular weight drug molecules can diffuse much more rapidly and penetrate deeper into tumor tissues (53). Furthermore, the tumor deposition and penetration of NDDS, especially those of T-BCMs and T-liposomes, can be improved by modifying the tumor physiology to further facilitate the EPR effect and their intratumoral transport. Some examples include co-delivery of extracellular matrix-degrading enzymes to promote tumor penetration, or vascular endothelial growth factor to enhance vascular permeability and reduce IFP (53,54). Indeed, the size of BCMs can also be reduced, by altering the properties of the copolymer, which may allow for improved mobility within tumor tissues and facilitate tumor penetration. Studies examining the impact of BCM particle size on their intratumoral transport are currently underway in our laboratory.

CONCLUSIONS

A firm understanding of the behavior and interactions of BCMs within their physiological environment is essential to effectively improving their performance as NDDS. Although we have demonstrated that active targeting can lead to a marginal increase in the total tumor accumulation of T-BCMs compared to NT-BCMs, we also learned that such an effect is heavily dependent on many other factors, such as passive targeting, tumor vascularization, tumor IFP, tumor penetration, *in vivo* cellular uptake and cell binding. As illustrated in the current study, problems such as limited tumor penetration, low levels of cell uptake, and continuous exocytosis of internalized BCMs pose significant barriers to achieving a therapeutically relevant active targeting effect *in vivo*. Therefore, more effort should be directed towards gaining an improved understanding of the physiological barriers that NDDS may encounter *in vivo*, in order to fully exploit their therapeutic potential.

ACKNOWLEDGMENTS

This study is supported by funding from Canadian Institutes of Health Research, Canadian Breast Cancer Research Alliance, and Ontario Institute for Cancer Research, awarded to C. Allen and R.M. Reilly. The authors are grateful to the Natural Sciences and Engineering Research Council of Canada, Hoffman-La Roche/Rosemarie Hager, and Lorne F. Lambier for scholarships awarded to H. Lee, as well as the MDS-Nordion Graduate Scholarship in Radiopharmaceutical Sciences awarded to B. Hoang. The authors would like to thank Deborah Scollard for technical assistance with the animal studies, as well as Anton Semechko from David A. Jaffray's Laboratory and STTARR core IV for technical support on the MATLAB® algorithm for the autoradiography studies.

REFERENCES

1. Matsumura Y, Kataoka K. Preclinical and clinical studies of anticancer agent-incorporating polymer micelles. Cancer Sci. 2009;100:572–9.
2. Torchilin VP. Recent advances with liposomes as pharmaceutical carriers. Nat Rev Drug Discov. 2005;4:145–60.
3. Maeda H, Bharate GY, Daruwalla J. Polymeric drugs for efficient tumor-targeted drug delivery based on EPR-effect. Eur J Pharm Biopharm. 2009;71:409–19.
4. Liu J, Lee H, Allen C. Formulation of drugs in block copolymer micelles: drug loading and release. Curr Pharm Des. 2006;12:4685–701.

5. Bae Y, Kataoka K. Intelligent polymeric micelles from functional poly(ethylene glycol)-poly(amino acid) block copolymers. Adv Drug Deliv Rev. 2009;61:768–84.
6. Moghimi SM, Hunter AC, Murray JC. Long-circulating and target-specific nanoparticles: theory to practice. Pharmacol Rev. 2001;53:283–318.
7. Li L, Wartchow CA, Danthi SN, Shen Z, Dechene N, Pease J, *et al.* A novel antiangiogenesis therapy using an integrin antagonist or anti-Flk-1 antibody coated 90Y-labeled nanoparticles. Int J Radiat Oncol Biol Phys. 2004;58:1215–27.
8. Gosk S, Moos T, Gottstein C, Bendas G. VCAM-1 directed immunoliposomes selectively target tumor vasculature *in vivo*. Biochim Biophys Acta. 2008;1778:854–63.
9. Kirpotin DB, Drummond DC, Shao Y, Shalaby MR, Hong K, Nielsen UB, *et al.* Antibody targeting of long-circulating lipidic nanoparticles does not increase tumor localization but does increase internalization in animal models. Cancer Res. 2006;66:6732–40.
10. Mamot C, Drummond DC, Noble CO, Kallab V, Guo Z, Hong K, *et al.* Epidermal growth factor receptor-targeted immunoliposomes significantly enhance the efficacy of multiple anticancer drugs *in vivo*. Cancer Res. 2005;65:11631–8.
11. Yoo HS, Park TG. Folate receptor targeted biodegradable polymeric doxorubicin micelles. J Control Release. 2004;96:273–83.
12. Sutton D, Nasongkla N, Blanco E, Gao J. Functionalized micellar systems for cancer targeted drug delivery. Pharm Res. 2007;24:1029–46.
13. Marcucci F, Lefoulon F. Active targeting with particulate drug carriers in tumor therapy: fundamentals and recent progress. Drug Discov Today. 2004;9:219–28.
14. Bae Y, Nishiyama N, Kataoka K. *In vivo* antitumor activity of the folate-conjugated pH-sensitive polymeric micelle selectively releasing adriamycin in the intracellular acidic compartments. Bioconjug Chem. 2007;18:1131–9.
15. Gabizon A, Horowitz AT, Goren D, Tzemach D, Shmeeda H, Zalipsky S. *In vivo* fate of folate-targeted polyethylene-glycol liposomes in tumor-bearing mice. Clin Cancer Res. 2003;9:6551–9.
16. Nobs L, Buchegger F, Gurny R, Allemann E. Biodegradable nanoparticles for direct or two-step tumor immunotargeting. Bioconjug Chem. 2006;17:139–45.
17. Lee H, Hu M, Reilly RM, Allen C. Apoptotic epidermal growth factor (EGF)-conjugated block copolymer micelles as a nanotechnology platform for targeted combination therapy. Mol Pharm. 2007;4:769–81.
18. Kullberg M, Mann K, Owens JL. Improved drug delivery to cancer cells: a method using magnetoliposomes that target epidermal growth factor receptors. Med Hypotheses. 2005;64:468–70.
19. Lee ES, Na K, Bae YH. Polymeric micelle for tumor pH and folate-mediated targeting. J Control Release. 2003;91:103–13.
20. Yoo HS, Park TG. Biodegradable polymeric micelles composed of doxorubicin conjugated PLGA-PEG block copolymer. J Control Release. 2001;70:63–70.
21. Park EK, Lee SB, Lee YM. Preparation and characterization of methoxy poly(ethylene glycol)/poly(epsilon-caprolactone) amphiphilic block copolymeric nanospheres for tumor-specific folate-mediated targeting of anticancer drugs. Biomaterials. 2005;26:1053–61.
22. Rampaul RS, Pinder SE, Nicholson RI, Gullick WJ, Robertson JF, Ellis IO. Clinical value of epidermal growth factor receptor expression in primary breast cancer. Adv Anat Pathol. 2005;12:271–3.
23. Mendelsohn J. The epidermal growth factor receptor as a target for cancer therapy. Endocr Relat Cancer. 2001;8:3–9.
24. Zeng F, Lee H, Allen C. Epidermal growth factor-conjugated poly(ethylene glycol)-block-poly(delta-valerolactone) copolymer micelles for targeted delivery of chemotherapeutics. Bioconjug Chem. 2006;17:399–409.
25. Hoang B, Lee H, Reilly RM, Allen C. Non-invasive monitoring of the fate of 111In-labeled block copolymer micelles by high resolution and high sensitivity MicroSPECT/CT imaging. Mol Pharm. 2009;6:581–92.
26. Zeng F, Allen C. Synthesis of carboxy-functionalized heterobifunctional poly(ethylene glycol) by a thiol-anionic polymerization method. Macromolecules. 2006;39:6391–8.
27. Hu M, Chen P, Wang J, Chan C, Scollard DA, Reilly RM. Site-specific conjugation of HIV-1 tat peptides to IgG: a potential route to construct radioimmunoconjugates for targeting intracellular and nuclear epitopes in cancer. Eur J Nucl Med Mol Imaging. 2006;33:301–10.
28. Costantini DL, Chan C, Cai Z, Vallis KA, Reilly RM. (111)In-labeled trastuzumab (Herceptin) modified with nuclear localization sequences (NLS): an Auger electron-emitting radiotherapeutic agent for HER2/neu-amplified breast cancer. J Nucl Med. 2007;48:1357–68.
29. Liu J, Zeng F, Allen C. *In vivo* fate of unimers and micelles of a poly(ethylene glycol)-block-poly(caprolactone) copolymer in mice following intravenous administration. Eur J Pharm Biopharm. 2007;65:309–19.
30. Wyckoff J, Wang W, Lin EY, Wang Y, Pixley F, Stanley ER, *et al.* A paracrine loop between tumor cells and macrophages is required for tumor cell migration in mammary tumors. Cancer Res. 2004;64:7022–9.
31. Dreher MR, Liu W, Michelich CR, Dewhirst MW, Yuan F, Chilkoti A. Tumor vascular permeability, accumulation, and penetration of macromolecular drug carriers. J Natl Cancer Inst. 2006;98:335–44.
32. Murphy KP, Xie D, Thompson KS, Amzel LM, Freire E. Entropy in biological binding processes: estimation of translational entropy loss. Proteins. 1994;18:63–7.
33. Rowinsky EK. The erbB family: targets for therapeutic development against cancer and therapeutic strategies using monoclonal antibodies and tyrosine kinase inhibitors. Annu Rev Med. 2004;55:433–57.
34. Carlin CR, Simon D, Mattison J, Knowles BB. Expression and biosynthetic variation of the epidermal growth factor receptor in human hepatocellular carcinoma-derived cell lines. Mol Cell Biol. 1988;8:25–34.
35. Fonge H, Lee H, Reilly RM, Allen C. Multifunctional block copolymer micelles for the delivery of 111In to EGFR-positive breast cancer cells for targeted auger electron radiotherapy. Mol Pharm. 2009. In Press.
36. Mikhail AS, Allen C. Block copolymer micelles for delivery of cancer therapy: transport at the whole body, tissue and cellular levels. J Control Release. 2009;138:214–23.
37. Yuan F, Dellian M, Fukumura D, Leunig M, Berk DA, Torchilin VP, *et al.* Vascular permeability in a human tumor xenograft: molecular size dependence and cutoff size. Cancer Res. 1995;55:3752–6.
38. McLarty K, Cornelissen B, Scollard DA, Done SJ, Chun K, Reilly RM. Associations between the uptake of 111In-DTPA-trastuzumab, HER2 density and response to trastuzumab (Herceptin) in athymic mice bearing subcutaneous human tumour xenografts. Eur J Nucl Med Mol Imaging. 2009;36:81–93.
39. Kuszyk BS, Corl FM, Franano FN, Bluemke DA, Hofmann LV, Fortman BJ, *et al.* Tumor transport physiology: implications for imaging and imaging-guided therapy. Am J Roentgenol. 2001;177:747–53.
40. Stohrer M, Boucher Y, Stangassinger M, Jain RK. Oncotic pressure in solid tumors is elevated. Cancer Res. 2000;60:4251–5.
41. Gao Y, Chen L, Gu W, Xi Y, Lin L, Li Y. Targeted nanoassembly loaded with docetaxel improves intracellular drug delivery and efficacy in murine breast cancer model. Mol Pharm. 2008;5:1044–54.
42. Park JS, Han TH, Lee KY, Han SS, Hwang JJ, Moon DH, *et al.* N-acetyl histidine-conjugated glycol chitosan self-assembled nanoparticles for intracytoplasmic delivery of drugs: endocytosis, exocytosis and drug release. J Control Release. 2006;115:37–45.
43. Panyam J, Labhasetwar V. Dynamics of endocytosis and exocytosis of poly(D, L-lactide-co-glycolide) nanoparticles in vascular smooth muscle cells. Pharm Res. 2003;20:212–20.
44. Fevrier B, Raposo G. Exosomes: endosomal-derived vesicles shipping extracellular messages. Curr Opin Cell Biol. 2004;16:415–21.
45. Maysinger D, Lovric J, Eisenberg A, Savic R. Fate of micelles and quantum dots in cells. Eur J Pharm Biopharm. 2007;65:270–81.
46. Barua S, Rege K. Cancer-cell-phenotype-dependent differential intracellular trafficking of unconjugated quantum dots. Small (Weinheim an der Bergstrasse, Germany). 2009;5:370–6.
47. Iero M, Valenti R, Huber V, Filipazzi P, Parmiani G, Fais S, *et al.* Tumour-released exosomes and their implications in cancer immunity. Cell Death Differ. 2008;15:80–8.

48. Salomon DS, Brandt R, Ciardiello F, Normanno N. Epidermal growth factor-related peptides and their receptors in human malignancies. Crit Rev Oncol Hematol. 1995;19:183–232.
49. Heber D. Nutritional oncology. Amsterdam: Elsevier-Academic Press; 2006.
50. Psaila B, Lyden D. The metastatic niche: adapting the foreign soil. Nat Rev Cancer. 2009;9:285–93.
51. Liu SQ, Tong YW, Yang YY. Incorporation and *in vitro* release of doxorubicin in thermally sensitive micelles made from poly(N-isopropylacrylamide-co-N, N-dimethylacrylamide)-b-poly(D, L-lactide-c o-glycolide) with varying compositions. Biomaterials. 2005;26:5064–74.
52. Rapoport N, Pitt WG, Sun H, Nelson JL. Drug delivery in polymeric micelles: from *in vitro* to *in vivo*. J Control Release. 2003;91:85–95.
53. Minchinton AI, Tannock IF. Drug penetration in solid tumours. Nat Rev Cancer. 2006;6:583–92.
54. Eikenes L, Tari M, Tufto I, Bruland OS, de Lange Davies C. Hyaluronidase induces a transcapillary pressure gradient and improves the distribution and uptake of liposomal doxorubicin (Caelyx) in human osteosarcoma xenografts. Br J Cancer. 2005;93:81–8.